SUPPORTING INFORMATION

Self-assembly based plasmonic arrays tuned by atomic layer deposition for extreme visible light absorption

Carl Hägglund,[*,†] *Gabriel Zeltzer,*[‡] *Ricardo Ruiz,*[‡] *Isabell Thomann,*[§] *Han-Bo-Ram Lee,*[†]

Mark L. Brongersma[§] *and Stacey F. Bent*[*,†]

[†]Department of Chemical Engineering, Stanford University, Stanford, CA
[‡]Hitachi Global Storage Technologies, San Jose, California
[§]Geballe Laboratory for Advanced Materials, Stanford University, Stanford, CA

[*]hagglund@stanford.edu, sbent@stanford.edu

Contents of supporting information:

SI:0 Methods

Sample fabrication overview

Samples were fabricated using a combination of thin film deposition techniques and block copolymer lithography (BCL, see further below). A polished 4" Si(100) wafer was coated by a 2 nm Ti adhesion layer and 90 nm Al by electron beam evaporation. A thin film of either 100 nm or 55 nm of SiO2 was deposited on top of the Al layer by ion beam deposition from a silicon oxide target and using oxygen-assist during deposition. Au nanodot arrays were subsequently fabricated using a combination of thin film deposition techniques and BCL. The resulting dots had diameters of approximately 17 nm and were distributed in dense hexagonal arrays with a lattice constant of about 38 nm. Hexagonal and square arrays of similar particle density and particle size were also made using electron beam lithography, but were used only for brief comparison in this work so their fabrication are not detailed further. Both nanodot patterned and unpatterned 4" Si wafers with identical spacer/reflector stacks on top were cut into smaller pieces and coated by thin films of varying thicknesses by means of atomic layer deposition (ALD, see further below).

Block copolymer lithography

A dense array of hexagonally packed Au nanodots placed on top of the SiO_2 spacer was produced by a liftoff technique using block copolymer lithography. First, a block copolymer sacrificial mask was formed following methods described elsewhere.[1-2] We used a cylinder-forming poly(styrene-b-methyl methacrylate) diblock copolymer (PS-b-PMMA, Polymer Source Inc, M_N = 65Kg/mol, M_W/M_N = 1.07, 69% by mass PS) which self-assembles into PMMA cylindrical domains in a PS matrix having a hexagonal packing with a center-to-center pitch of 38 nm.

In order to promote a perpendicular orientation of the PMMA cylinders with respect to the surface of the substrate, a surface with neutral interaction to the block copolymer was created by grafting a thin layer of hydroxyl-terminated polystyrene-ran-poly(methyl methacrylate) M_N = 8 kg/mol, 63% by mass PS by spin coating and annealing at 200 ^{o}C in vacuum for 1 h. Unbound material was then rinsed with toluene. A ~40 nm thick block copolymer film was deposited by spin coating from a toluene solution on top of the neutral layer and annealed in vacuum at 220 ^{o}C for 1 h. During annealing the block copolymer film self assembles into an array of PMMA cylinders perpendicularly oriented to the substrate. To selectively remove the PMMA, UV light exposure for 7 min was used to scission the PMMA chains and cross link the PS. The PMMA dissolved in acetic acid for 3 min.[3] Remaining PS mask was partially etched with oxygen plasma to clean the bottom of the pores.

For the set of samples using a 100 nm SiO_2 spacer, a 2 nm layer of Ta followed by 5 nm of Au was deposited on top of the PS mask by ion beam deposition. Samples having a 55 nm SiO_2

spacer used a 1 nm Ta followed by 7 nm of Au. The PS mask was lifted off in piranha solution (H_2SO_4 + H_2O_2, 2:1 volume ratio) at 120 °C for 5 min. The result after liftoff is an array of Ta/Au dots 17-18 nm in diameter with a 38 nm pitch. Note that the Au dots contracted into higher, more thermodynamically stable spheriodal shapes in this process. The Ta below the Au likely oxidized upon exposure to piranha and air, but can possibly be distinguished underneath the particles in close-up TEM images (Fig. 2f,h).

Atomic layer deposition

Thin films of tin sulfide (SnS_x) were deposited using tetrakis(dimethylamino)tin(IV) (TDMASn, STREM Chemicals, >99% purity) and H_2S as precursors. The H_2S was generated in a separate vial through thermal decomposition of thioacetamide (Sigma-Aldrich, >99% purity).[4] Precursor vapors were pulsed sequentially into a homebuilt viscous flow reactor with in situ stage temperature monitoring and an online mass spectrometer to control gas composition. A substrate temperature of 110° C was used, at which the optical properties of uncoated Au dot arrays were found stable. ALD cycles of 1 s TDMASn/30 s purge/0.25 s H_2S/15 s purge was employed with a continuous flow of 10 SCCM N_2 as a carrier and purge gas, yielding a growth rate of 1.3 SnS_x Å/cycle. Thin film X-ray diffraction measurements conducted at the Stanford Synchrotron Radiation Lightsource (SLAC) indicated that the resulting tin sulfide film was amorphous. X-ray photoelectron spectroscopy (XPS) showed no residual carbon or nitrogen after a brief Ar sputtering to remove surface contamination. Comparison of the XPS data to that of pure SnS powder suggested a film stoichiometry closer to SnS_2 than to SnS. This composition is expected based on the tin precursor oxidation state, and further consistent with the optical properties (Figure S1) of SnS_2.[5]

ALD of polycrystalline ZnO films followed an established route[6-7] using diethylzinc (DEZn, Sigma-Aldrich) and deionized water as precursors. The substrate was kept at 100° C and a cycle of 1 s DEZn/15 s purge/1 s H_2O/30 s purge was employed with a continuous flow of 10 SCCM N_2. The film growth rate was measured to be 1.7 Å/cycle.

Finally, ALD of Al_2O_3 films used trimethylaluminum (TMA, Sigma-Aldrich) and deionized water as precursors, following a route known to produce highly uniform layers of x-ray amorphous Al_2O_3.[8-9] The substrate temperature was 100° C and a cycle of 0.5 s TMA/15 s purge/1 s H_2O/30 s purge was used. A growth rate of 1.1 Å/cycle was observed.

Spectroscopic ellipsometry

Spectroscopic ellipsometry measurements were performed using a Woollam M2000 instrument. Data was collected for photon energies of 0.74 to 5.89 eV and at angles of incidence of 65°, 70° and 75°. The incident beam was linear polarized at 45° from the plane of incidence.

The layers of SiO$_2$ and Al were analyzed prior to deposition of the plasmonic arrays. Ellipsometric measurements were performed for 5 different locations on the 4" wafer coated with SiO$_2$ on top of the Al. The ellipsometric data was analyzed using a stratified model including three isotropic, homogeneous layers. The bottom, optically thick Al layer, used tabulated optical constants.[10] Between the Al and SiO$_2$, an intermix layer accounting for interfacial roughness was included. This used the Bruggeman effective medium approximation, fitting the volume fraction of Al and the depolarization factor. Finally, the SiO$_2$ layer was represented by a single Lorentzian accounting for absorption in the UV, centered around 4.5 eV. Further UV absorption outside the measured interval was taken into account by a Sellmeier term. A constant offset for the real part of the permittivity was also included, giving a total of 6 fitting parameters for the SiO$_2$ optical constants. The optical constants of the SiO$_2$ spacer and SiO$_2$/Al intermix layer were fitted along with the thicknesses by minimizing the root mean square error (MSE) in comparison with the collective data set (in N,C,S functions[11]), comprising a total of 15 ellipsometric spectra spanning 695 wavelengths each for the different locations and angles of incidence.

SE was subsequently performed on bare and coated plasmonic arrays fabricated on top of the SiO$_2$, while keeping the predetermined properties of the Al/SiO$_2$ layers fixed. The arrays were represented by a single, homogeneous and isotropic layer, with optical properties modeled as a sum of oscillator terms positioned in different spectral regions. The response around the plasmon resonance was fitted by a sum of a harmonic and a Gaussian oscillator, as a significantly lower MSE could be achieved in this way than, for instance, with a single Lorentzian. The UV response near the bandgap thresholds of the coatings was mainly accounted for by a "psemi-m0" polynomial spline function.[11] An additional harmonic oscillator term accounted for absorption at higher energies in the SnS$_x$ and ZnO coatings. IR and UV-poles (Sellmeier terms) were also included along with a constant offset of the real part of the permittivity. Altogether, the MSE was minimized by fitting 18 parameters including the effective thickness of the layer. The resulting optical constants were Kramers-Kronig consistent by construction.

Laser reflectance measurements

Reflectance at near-normal (approximately 2°) angle of incidence was measured from 450 to 750 nm in steps of 5 nm, using a supercontinuum white-light source (Fianium) coupled to an acousto-optical tunable filter with a transmission bandwidth of 5 nm and a silicon photodetector. The reflected intensity I was referenced to the reflected intensity I_{ref} from a silver mirror (ThorLabs P01) with tabulated reflectance R_{ref}, yielding the sample reflectance according to $R = I / I_{ref} \times R_{ref}$.

SI:1 Analysis of non-ideal reflectors

At a planar interface between two media with (complex) refractive indices m_1 and m_2, the electric field of normal incident light undergoes reflection according to the Fresnel reflection coefficient[12]

$$r = |r|e^{i\phi} = \frac{m_1 - m_2}{m_1 + m_2}. \qquad (S1)$$

For light incident from a dielectric ($\mathrm{Re}\, m_1 > 0$) onto a perfect electric conductor ($m_2 \rightarrow i\infty$), the reflection coefficient is -1 and the phase shift $\phi = -\pi$ rad. Compared to such an ideal reflector, a metal reflector and its surface roughness creates a slightly less negative phase shift of the reflected wave, as well as a reduced reflection amplitude. To account for the effect of the modified phase shift in equation (1) of the main text, the reflection coefficient of the interface is first required. We take roughness at this interface into account by fitting an inserted Bruggeman effective medium layer (see Fig. 1d and Methods) with a complex refractive index m_B and thickness d_B between the spacer and solid metal. Defining the Fresnel coefficients r_1 and r_2 for the front and back interface of this intermix layer, respectively, the total reflection coefficient of the interface can be written as[12] $\tilde{r} = (r_1 - r_2\gamma^2)/(1 - r_1 r_2 \gamma^2)$, where $\gamma = \exp(2\pi i m_B d_B / \lambda_0)$. The phase shift difference relative the perfect reflector is then obtained from $\Delta\phi = \arg(\tilde{r}) + \pi$ rad. To compensate for the phase shift difference in the analytical model, the corresponding optical path length is added to the spacer by taking $h \rightarrow h + \Delta h$ in equation (1), with $\Delta h = \lambda_0 /(4\pi n_s) \times \Delta\phi$.

For the Al reflector used in this work, the phase shift difference at normal incidence of light at 600 nm wavelength is found to correspond to an extra SiO_2 spacer thickness of 13.8 nm, of which 1.1 nm stems from the interfacial roughness and the reminder from the bulk optical properties of Al.

SI:2 Optical constants of ALD coatings

Figure S1 shows the spectral dependence of the optical constants of a series of ALD deposited films of increasing thickness as deposited. These films were deposited on substrates identical to those used for the Au dot arrays, that is with a SiO_2 spacer and Al reflector. The films were deposited during the same ALD run as the Au dot array coatings. The SnS_x coatings of Fig. S1a,b behave and look similar, suggesting that the analysis does not artificially depend on the spacer thickness (being 100 nm in Fig. S1a and 55 nm in b, respectively). The dependence of the optical constants on thickness can be expected in this thickness range if, for instance, the film growth proceeds via nucleation at specific surface sites, island type growth and a gradual formation of a more uniform thickness layer, a dependence of the optical constants on thickness can be expected in this thickness range.

The extinction coefficients of the Al_2O_3 films were negligible in the visible range, but a weak absorption onset was observed around 4.4 eV (that is around 275 nm wavelength, outside the range included in the plots), although the actual optical bandgap of Al_2O_3 is typically at 6.4 eV (outside our measurement range). This finding is consistent with some previous observations.[13]
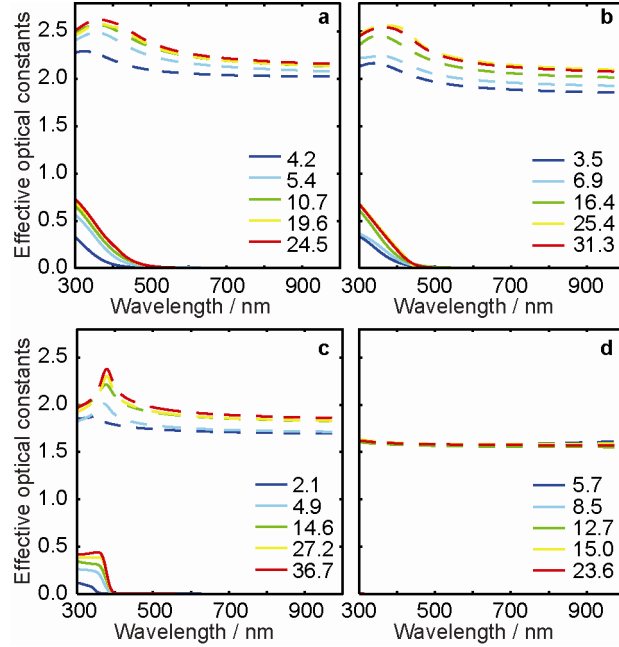

FIGURE S1. Optical constants determined by spectroscopic ellipsometry for ultrathin ALD films of SnS_x, ZnO and Al_2O_3. The real part of the refractive index is shown by dashed lines and the imaginary part (the extinction coefficient) by solid lines. Film thicknesses are given in nanometers in the legends. (a) SnS_x optical constants for films deposited on a 100 nm SiO_2 spacer. (b) SnS_x optical constants for films deposited on a 55 nm SiO_2 spacer. (c) ZnO optical constants for films deposited on a 55 nm SiO_2 spacer. (d) Al_2O_3 optical constants for films deposited on a 55 nm SiO_2 spacer.

SI:3 Comparison of normal incidence reflectance measurements

To check the degree to which our assumption of isotropic array properties in the SE model are useful, the reflectance for normal incident light was calculated and compared to measurements using a supercontinuum fiber laser at an angle of incidence of about 2° (Figure S2). The deviation between the minimum reflectance from the laser measurements and the SE model was less than 0.5% for the two most strongly absorbing SnS_x and ZnO coated arrays, when the measurements were done within a few days time (Fig. S2c,f). Over the course of months, the SnS_x peak blue shifted slightly, as seen by comparison of Fig. S2e and f. These results suggest that the normal incidence absorptance ($A \approx 1 - R$) in the coated arrays, as

calculated from the SE model, is accurate to within 0.5% absolute error at the peaks. Figure S2 also provides the SE derived absorptance in the Al reflector layer. It is 5 to 6% at the least reflective conditions, where the overall reflectance is below 1%. The SiO_2 absorptance is negligible (see further Fig. 4 of the main text).
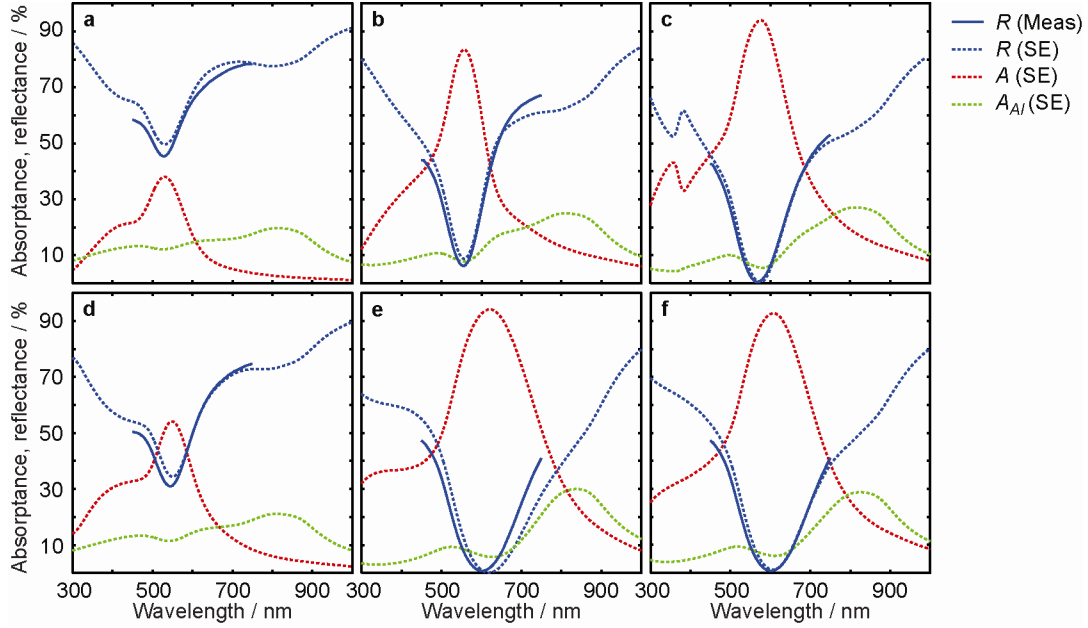

FIGURE S2. Laser measured normal incidence reflectance versus ellipsometry model reflectance and absorptance. The sample reflectance R (Meas) was measured using a tunable laser source at near normal incidence and compared to the calculated reflectance R (SE) based on the spectroscopic ellipsometry model fitted for each sample. The SE determined absorptance in the coated array A (SE) and in the Al reflector A_{Al} (SE) are also shown. The samples used a 55 nm SiO_2 spacer and were in (a) a bare Au nanodot array, (b) a 15.4 nm Al_2O_3 coated array, (c) a 14.6 nm ZnO coated array, (d) a 3.5 nm SnS_x coated array, (e) a 16.4 nm SnS_x coated array and in (f) the same 16.4 nm SnS_x coated array with SE done shortly after the reflectance measurement.

SI:4 Dependence of absorptance on optical parameters in contour plots

To clarify why the maximum array absorptance increases when the spacer thickness is reduced to 55 nm and the Au content in the array is increased, a fixed effective film thickness and wavelength may be considered, so that absorptance contour plots versus the effective optical constants of the film can be obtained (Fig. S3). We used the finite element method (with software from Comsol Multiphysics[14]) to numerically calculate the absorption as a function of the absorber layer optical constants and to interpolate the maxima, but as this problem is in one dimension of space, it can also be solved through recurrence formulas[15] or by means of the

transfer matrix method.[16] The optima predicted by equation (1) of the main text after compensation for reflection phase shift as described in SI:1, are seen to be in excellent agreement with the optima obtained numerically.

The optical constants of the most absorbing samples can be directly compared to the overall optima by choosing the conditions of the plots according to the effective thickness d_{eff} of the coated arrays and by using their peak wavelengths. To include data for other ALD coating thicknesses, and therefore other peak wavelengths and effective array thicknesses, we used equation (1) to project their optical constants according to $m_{eff}' = m_{eff} \, m_{ideal}' / m_{ideal}$, where unprimed (primed) variables correspond to the original peak (targeted contour plot) wavelength and thickness. This transforms the optical constants according to the dependence of the analytical model optimum and is confirmed to yield similar peak absorption rates in the maps (Fig. S3) as in the original calculations (Fig. 3c,f,i and l of the main text).

Fig. S3a illustrate how the effects of reduced spacer thickness and increased effective array thickness combine to bring the optimum closer to the effective optical constants attainable by the SnS_x coated arrays. To leading order in equation (1), the reduced spacer thickness shifts the optimum towards a higher real part of the permittivity ($n_{eff}^2 - k_{eff}^2$) while the increased effective thickness reduces the optimal damping ($2n_{eff} \, k_{eff}$) of the absorber.[17] With the 55 nm spacer, almost perfect tuning of the sample properties to the overall optimum can thereby be achieved (Fig. S3b), leading to the maximum 94% array absorptance. The situation is similar with the ZnO coated arrays (Fig. S3c) and Al_2O_3 coated arrays (Fig. S3d), although in the latter case the refractive index of the Al_2O_3 is not enough to tune the array quite as close to the overall optimum.
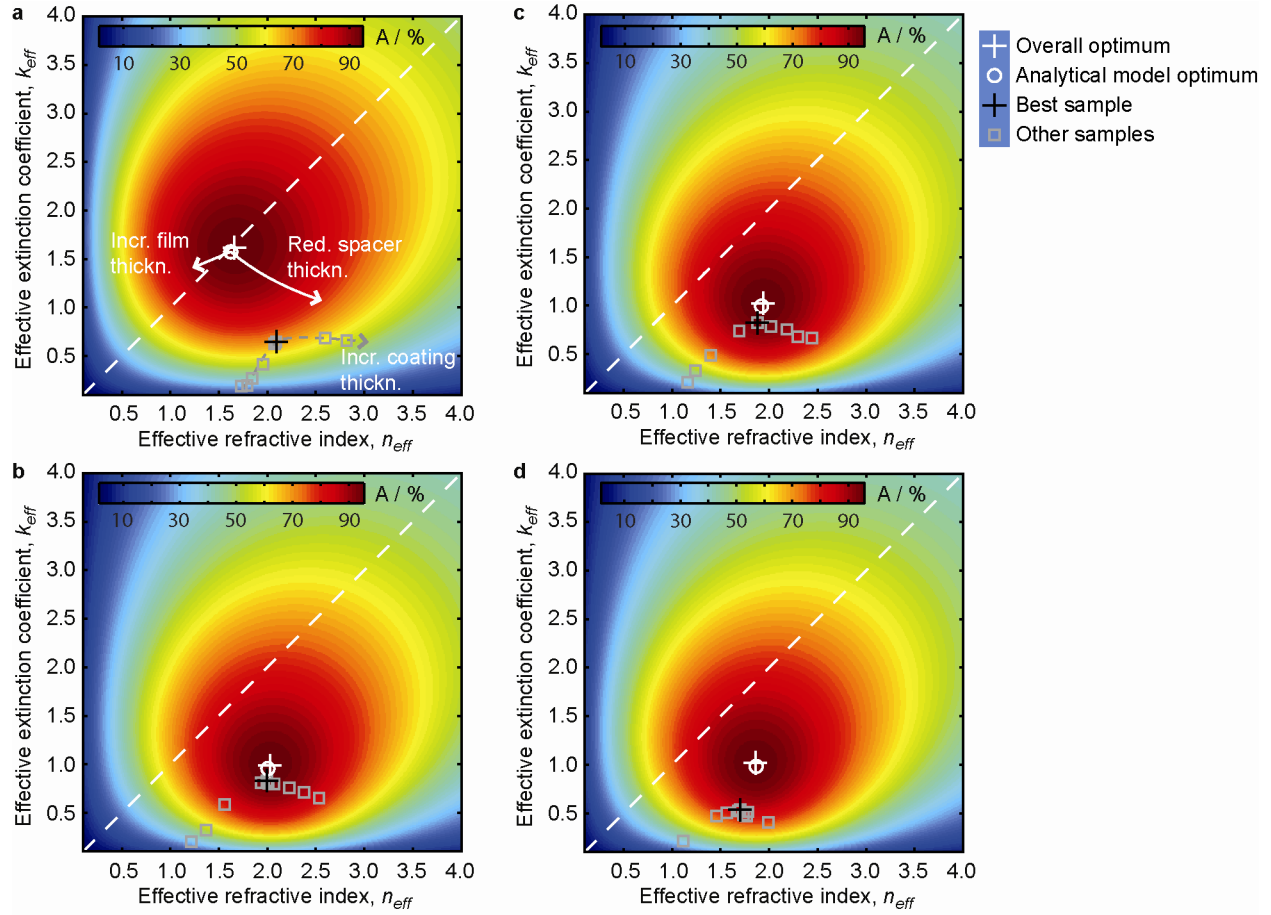
FIGURE S3. Absorptance in ultrathin films on a SiO_2 spacer/Al reflector as a function of the (effective) thin film optical constants. The conditions used correspond to the best (most absorbing) sample of each type, with their effective optical constants indicated by black crosses. The gray squares show the projected optical constants for samples with coating thicknesses other than the best. The sample types are, in (a) SnS_x coated arrays on a 100 nm SiO_2 spacer, (b) SnS_x coated arrays on a 55 nm spacer, (c) ZnO coated arrays on a 55 nm spacer and (d) Al_2O_3 coated arrays on a 55 nm spacer. The overall optima (white crosses) are well predicted by the analytical model (white circles). The dashed white line show $n_{eff} = k_{eff}$, close to which the optimum would be located with a quarterwave spacer. In (a) the curved white arrow indicates the translation of the ideal optimum when the spacer thickness is reduced, while the shorter white arrow shows its translation if the film thickness is increased. The gray arrow indicates the sample property changes with increasing coating thickness.

SI:5 Sample reflectance and local absorption rates by FEM calculations

In order to estimate the absorption rate distribution in the Au versus in the ALD coating materials, calculations by the finite element method (FEM) were performed for three dimensional geometries simulating the highest absorbing SnS_x and ZnO samples on the 55 nm SiO_2 spacer, see Fig. 4 of the main text. The basic procedure was previously described[18] and used software from Comsol Multiphysics.[14] The unit cell illustrated in Fig. 4b of the main text was used to simulate the array with periodic boundary conditions (perfect electric and perfect magnetic conductors) on the *y*- and *z*-plane boundaries, respectively. The geometry was terminated backwards by a perfectly matched layer simulating infinity (zero reflectance), and in the forward direction by an impedance boundary condition simulating an interface with aluminum,[10] which here represents the optically thick reflector layer. The properties and thickness of the SiO_2 spacer layer and the Bruggeman SiO_2/Al effective medium approximation for the intermix layer were taken from the spectroscopic ellipsometry analysis of these layers, as described in the Methods section of the main text.

The array geometry was based on the dimensions observed in the electron micrographs. The particles were approximated as oblate spheroids with diameters of 16.8 nm and heights of 13.6 nm, as observed by TEM. They were distributed in an array with a lattice constant of 37.9 nm, as observed by SEM. The coatings were given a corrugation as shown in Fig. S2b,c, in rough agreement with the TEM images, and such that their average height agreed with the effective thickness of the arrays found by ellipsometry (27.7 and 25.6 nm for the SnS_x and ZnO coated arrays, respectively). These heights were similar to the average heights of the coated arrays found by the TEM analyses. The Ta adhesion layer (1 nm deposited) underneath the Au was not included explicitly as it was likely oxidized and not clearly distinguished by TEM. Amorphous, low temperature deposited TaO has a bandgap exceeding 4 eV and shows negligible absorption in the visible with a real refractive index around 2.1 at 600 nm.[19] To represent this situation, a 1 nm gap was introduced between the Au particles and the SiO_2 spacer, which was for simplicity filled by the coating (SnS_x or ZnO) since these had optical properties similar to TaO. This simplification somewhat overestimates the absorption in the coating part of the arrays compared to that in the Au part.

The optical constants of bulk Au were taken from tabulated values.[20] An additional term was included to account for surface scattering. The latter was implemented according to equation (1).4 of ref. [21] with a prefactor *A* of unity and the effective inelastic mean free path $l_{eff} = 4V/S$, with *S* being the metal particle surface area and *V* its volume. The properties of Au were further represented by a bulk inelastic mean free path of 50 nm based on its direct current conductivity, a bulk plasmon resonance energy of 9.01 eV, and a Fermi velocity of 1.39×10^6 m/s. The optical constants of the ALD coatings were taken from the SE analysis (Fig. S1) of unpatterned samples coated during the same ALD runs.

Given that no parameters were fitted in these calculations, the agreement with regards to peak position and peak absorptance is very good for both SnS_x and ZnO coated samples, with only a slight redshift compared to the SE determined response (Fig. 4d,e). A lower peak width in

the FEM calculations can be attributed to, for instance, inhomogeneities in particle size and shape and the somewhat rough substrate which leads to a height distribution of the particles. The contribution to the peak width from surface scattering/chemical interface damping could also be somewhat higher than assumed here, but should not be dramatically different as this would have a negative impact on the peak amplitude. Therefore, it appears feasible that the FEM calculated absorption in the different parts of the array are reasonable estimates of the actual situation. Table S1 summarizes key numbers extracted from the FEM calculations at the peak wavelengths, through volume integration of the local absorption rates in the Au (A_{Au}) and array coating (A_{Coat}), respectively. The branching ratio for incident light absorption in the Au nanodots versus in the coated array is calculated as $\gamma_{Au} = A_{Au} / A$, using the FEM calculated coated array absorption $A(\text{FEM}) = A_{Au}(\text{FEM}) + A_{Coat}(\text{FEM})$. An estimate for the fraction of light absorbed in the Au part of the coated array is then obtained from $A_{Au} = \gamma_{Au} A(\text{SE})$ where the $A(\text{SE})$ is the array absorption calculated from the spectroscopic ellipsometry model. The full absorption spectrum of the array constituents are shown together with the spacer absorptance in Fig. 4e,f of the main text.

TABLE S1. Array absorption distribution

Array coating material	A_{Coat} / % (FEM)	A_{Au} / % (FEM)	Γ_{Au} / % (FEM)	A / % (SE)	A_{Au} / % (SE & FEM)
SnS$_x$	1.8	93.0	98.1	94.2	92.4
ZnO	0.6	93.4	99.4	94.0	93.4

SI:6 Comparison with the optical *f*-sum rule

The results and their attribution to the localized surface plasmon of the Au nanodots are compatible with the optical *f*-sum rule for the imaginary part of the (effective) array permittivity. This constitutes a physical limit on the oscillator strength based on the number of conduction electrons in the array, expressed as[22]

$$\int_0^\infty \omega \operatorname{Im} \varepsilon_{eff}\, d\omega = \frac{\pi}{2} \omega_p^2 , \qquad (S2)$$

where ω_p is the effective bulk plasma frequency of the material, $\omega_p^2 = n_e e^2 / \varepsilon_0 m^*$, for an electron density n_e and effective electron mass m^*. To consider the partial contribution to the integral from the localized surface plasmon resonance, the resonance peak of the spectrum was fitted by a harmonic oscillator function, $\operatorname{Im} \varepsilon_{plas} = A_0 \Gamma^2 \omega_0 \omega / [(\omega_0^2 - \omega^2 + \Gamma^2 / 4)^2 + \Gamma^2 \omega^2]$, where ω_0 is its center frequency, A_0 amplitude and Γ width, see Fig. 5a in the main article. For the harmonic oscillator, the integral simply yields $\pi / 2 \times \omega_0 A_0 \Gamma$. For the right hand side of equation (S2), we assume that the electrons contributing to the plasmon resonance are the conduction electrons of

the Au (density $n_{e,Au}$), with its volume equivalent film thickness d_{eq}=1.6 nm. An effective electron density of the film is obtained by dividing their number by the effective film thickness d_{eff}, so that the ratio formed by the left and right hand side, $\omega_0 A_0 \Gamma \big/ [n_{e,Au} e^2 d_{eq} /(d_{eff}\varepsilon_0 m^*)]$, is a measure of the fraction of the Au conduction electron oscillator strength engaged in the plasmon resonance. Using $n_{e,Au}$=5.9×10^{22} cm^{-3} for Au[23] and an effective mass equal to the free electron mass,[24] this ratio is what is plotted in Fig. 5b as a function of ALD coating thickness. In contrast to the peak absorptance, which is maximized for the particular coating thickness generating conditions closest to critical coupling (see Fig. 5c and further Fig. S3), the plasmon oscillator strength is seen to saturate above a certain coating thickness (Fig. 5b). For the most absorbing samples, it reaches almost 70% of the full oscillator strength associated with the Au conduction electrons, showing that our results can be fully interpreted as absorption in the Au. The saturation can be understood since the plasmon resonance will, beyond a certain coating thickness, not change its contribution to the polarizability. When the effective thickness of the array increases, its contribution to the effective medium properties will be diluted in inverse proportion. On the other hand, in assuming that only Au contributes to the effective electron density and ω_p^2, there is a corresponding reduction of the right hand side of equation (S2), so that the ratio of oscillator strength must saturate. That this saturation is observed is a further support that the coatings do not contribute significantly in themselves to the absorption of the plasmon resonance; if they were, the ratio would keep increasing under our assumption.

It is also noteworthy that the saturation level for the oscillator strength condensed into the plasmon resonance increases with increasing refractive index of the coatings. Apart from the mentioned effect of the surrounding medium dielectric constant on the particle dipole polarizability at resonance, another contribution could stem from the redshift of the peak. This leads to reduced spectral overlap with the Landau damping associated with interband transitions in Au around 2.4 eV,[25] which compete with the plasmon resonance for oscillator strength. A more detailed analysis would however be required to bring full clarity to this.

Supporting References

1   Hellwig, O. *et al.* Bit patterned media based on block copolymer directed assembly with narrow magnetic switching field distribution. *Appl. Phys. Lett.* **96**, 052511, doi:10.1063/1.3293301 (2010).
2   Bosworth, J. K., Dobisz, E. A., Hellwig, O. & Ruiz, R. Impact of Out-of-Plane Translational Order in Block Copolymer Lithography. *Macromolecules* **44**, 9196-9204, doi:10.1021/ma201967a (2011).
3   Thurn-Albrecht, T. *et al.* Nanoscopic Templates from Oriented Block Copolymer Films. *Adv. Mater.* **12**, 787-791, doi:10.1002/(sici)1521-4095(200006)12:11<787::aid-adma787>3.0.co;2-1 (2000).
4   Bakke, J. R., King, J. S., Jung, H. J., Sinclair, R. & Bent, S. F. Atomic layer deposition of ZnS via in situ production of H2S. *Thin Solid Films* **518**, 5400-5408, doi:10.1016/j.tsf.2010.03.074 (2010).

5   Vol. 41C *Landolt-Börnstein - Group III Condensed Matter* eds O. Madelung, U. Rössler, & M. Schulz) (Springer, 2012).

6   Guziewicz, E. *et al.* ZnO grown by atomic layer deposition: A material for transparent electronics and organic heterojunctions. *J. Appl. Phys.* **105**, 122413, doi:10.1063/1.3133803 (2009).

7   Tanskanen, J. T., Bakke, J. R., Pakkanen, T. A. & Bent, S. F. Influence of organozinc ligand design on growth and material properties of ZnS and ZnO deposited by atomic layer deposition. *Journal of Vacuum Science & Technology A: Vacuum, Surfaces, and Films* **29**, 031507, doi:10.1116/1.3572232 (2011).

8   Grigoras, K., Franssila, S. & Airaksinen, V. M. Investigation of sub-nm ALD aluminum oxide films by plasma assisted etch-through. *Thin Solid Films* **516**, 5551-5556, doi:10.1016/j.tsf.2007.07.121 (2008).

9   Jakschik, S. *et al.* Crystallization behavior of thin ALD-Al2O3 films. *Thin Solid Films* **425**, 216-220, doi:10.1016/S0040-6090(02)01262-2 (2003).

10   Smith, D. Y., Shiles, E. & Inokuti, M. in *Handbook of Optical Constants of Solids* Vol. I (ed D. Palik Edward) 397-400 (Academic Press, 1997).

11   *Guide to using WVASE32*. (J. A. Woollam Co., Inc.).

12   Bohren, C. F. & Huffman, D. R. *Absorption and Scattering of Light by Small Particles*. (Wiley-VCH, 1998).

13   Kim, Y., Lee, S. M., Park, C. S., Lee, S. I. & Lee, M. Y. Substrate dependence on the optical properties of Al[sub 2]O[sub 3] films grown by atomic layer deposition. *Appl. Phys. Lett.* **71**, 3604-3606, doi:10.1063/1.120454 (1997).

14   Comsol Multiphysics. <http://www.comsol.com/> (2012).

15   Chew, W. C. *Waves and fields in inhomogeneous media*. (Van Nostrand Reinhold, 1990).

16   Born, M. & Wolf, E. *Principles of Optics: Electromagnetic Theory of Propagation, Interference and Diffraction of Light*. (Cambridge University Press, 1999).

17   Hägglund, C. & Apell, S. P. Plasmonic near-field absorbers for ultrathin solar cells. *The Journal of Physical Chemistry Letters* **3**, 1275-1285, doi:10.1021/jz300290d (2012).

18   Hägglund, C., Zäch, M., Petersson, G. & Kasemo, B. Electromagnetic coupling of light into a silicon solar cell by nanodisk plasmons. *Appl. Phys. Lett.* **92**, 053110, doi:10.1063/1.2840676 (2008).

19   Franke, E., Schubert, M., Trimble, C. L., DeVries, M. J. & Woollam, J. A. Optical properties of amorphous and polycrystalline tantalum oxide thin films measured by spectroscopic ellipsometry from 0.03 to 8.5 eV. *Thin Solid Films* **388**, 283-289, doi:10.1016/S0040-6090(00)01881-2 (2001).

20   Weaver, J. H. & Frederikse, H. P. R. in *CRC Handbook of Chemistry and Physics*   (ed David R Lide) (CRC Press, Boca Raton, FL, 2002).

21   Coronado, E. A. & Schatz, G. C. Surface plasmon broadening for arbitrary shape nanoparticles: A geometrical probability approach. *J. Chem. Phys.* **119**, 3926-3934, doi:10.1063/1.1587686 (2003).

22   Smith, D. Y. & Shiles, E. Finite-energy f-sum rules for valence electrons. *Phys. Rev. B* **17**, 4689-4694, doi:10.1103/PhysRevB.17.4689 (1978).

23   Lide, D. R. in *CRC Handbook of Chemistry and Physics, Internet version*   (Taylor and Francis, Boca Raton, Fl, 2007).

24   Szczyrbowski, J. A new simple method of determining the effective mass of an electron or the thickness of thin metal films. *Journal of Physics D: Applied Physics* **19**, 1257, doi:10.1088/0022-3727/19/7/015 (1986).

25   Alvarez, M. M. *et al.* Optical Absorption Spectra of Nanocrystal Gold Molecules. *The Journal of Physical Chemistry B* **101**, 3706-3712, doi:10.1021/jp962922n (1997).